

Off-axis interferometer with adjustable fringe contrast based on polarization encoding

Sharon Karepov,^{1,2,*} Natan T. Shaked,² and Tal Ellenbogen¹

¹Department of Physical Electronics, Faculty of Engineering, Tel-Aviv University, Tel-Aviv 69978, Israel

²Department of Biomedical Engineering, Faculty of Engineering, Tel-Aviv University, Tel-Aviv 69978, Israel

*Corresponding author: sharond3@post.tau.ac.il

Received January 12, 2015; revised March 27, 2015; accepted April 1, 2015;
posted April 3, 2015 (Doc. ID 232118); published May 7, 2015

We propose a compact, close-to-common-path, off-axis interferometric system for low polarizing samples based on a spatial polarization encoder that is placed at the Fourier plane after the output port of a conventional transmission microscope. The polarization encoder erases the sample information from one polarization state and maintains it on the orthogonal polarization state while retaining the low spatial frequencies of the sample, and thus enabling quantitative phase acquisition. In addition, the interference fringe visibility can be controlled by polarization manipulations. We demonstrate this concept experimentally by quantitative phase imaging of a USAF 1951 phase test target and human red blood cells, with optimal fringe visibility and a single-exposure phase reconstruction. © 2015 Optical Society of America

OCIS codes: (090.1995) Digital holography; (100.3175) Interferometric imaging; (130.5440) Polarization-selective devices; (170.3880) Medical and biological imaging; (180.3170) Interference microscopy.

<http://dx.doi.org/10.1364/OL.40.002273>

Interferometric phase microscopy (IPM), also known as digital holographic microscopy, enables to quantitatively measure optical path differences in transparent or translucent microscopic samples [1–7]. Relevant applications are biological cell imaging [5,6,8] and optical metrology [9,10]. After the spatial interference pattern is recorded by a digital camera, one can digitally extract the optical path delay (OPD) map of the sample [2,3,11]. The OPD map is equal to the product of the local physical thickness and the relative refractive index contents of the sample. The lateral resolution of this map is diffraction limited, while the axial precision is nanometric [2,10,12]. By using off-axis interferometry, only a single camera exposure is needed for obtaining the OPD map, so that dynamic samples can be acquired [13–19].

A major parameter that controls the OPD accuracy is the interference fringe contrast. Poor fringe contrast results in insufficient phase modulation depth, decreasing the signal-to-noise ratio, and essentially deteriorating the quality of the OPD maps [20,21].

Another major parameter that influences the OPD accuracy is the degree of the common path shared by the two interfering beams. Ideally, the reconstructed OPD represents only the delay acquired in the sample; thus, it is desired that both reference and sample beams go through the same optical path, excluding the sample itself. This configuration is known as common-path geometry, and aids in increasing the temporal stability of the OPD signal. A close-to-common-path configuration is achieved by separating the reference beam from the sample beam as closely as possible to the interference plane [3].

In this Letter, we propose an off-axis polarization-encoded interferometer (PEI) for quantitatively imaging low-polarizing samples within a single camera exposure and with adjustable fringe contrast. In this compact interferometer, the sample information is encoded on one polarization state and filtered from the orthogonal polarization state, serving as the reference beam.

Similarly to the proposed PEI, point diffraction interferometers [22] also generate the reference arm by

filtering high spatial frequencies. However, the sample beam does not contain the undiffracted light. In contrast, the proposed PEI retains this light so that its sample beam also contains the low spatial frequencies of the sample. This is important for quantitative phase map reconstruction. Using a birefringent beam displacer, we enable off-axis interference on the camera, and thus a complete OPD map reconstruction from a single interferogram, allowing imaging of highly dynamic samples.

In comparison to conventional interferometers, the sample and reference beams in the proposed PEI travel inseparably through almost the entire system, in a close-to-common-path geometry. Finally, the PEI allows optimizing the fringe contrast by setting the polarization of the incident or output light to achieve optimal ratio between the reference and sample beams.

Figure 1 presents the measurement setup. The first part of the setup is an inverted transmission microscope, illuminated by a linearly polarized Helium-Neon (HeNe) laser (632.8 nm wavelength). In the inverted microscope, the input light polarization is controlled by a quarter wave plate (QWP), followed by a rotating polarizer (RP). The QWP converts the linear polarization of the laser into circular polarization; hence, it enables maintaining constant power, regardless of the polarization angle of the RP. The polarized light is then transmitted through the sample to a microscope objective (20 \times , 0.42 numerical aperture, infinity corrected), followed by a compatible tube lens (200 mm focal length), which forms the output magnified image of the microscope. At the output of the microscope, the portable PEI module (marked by a dashed blue rectangle in Fig. 1) is connected. The PEI module consists of a Fourier transforming lens FTL (100 mm focal length) with a subsequent polarization encoding spatial filter (PE) placed at the Fourier plane. The PE is made of a 0.3 mm thick polyvinyl alcohol polarizing film sheet (extinction ratio 1000:1 at 632.8 nm). A focused laser beam, with intensity above the damage threshold of the polarizer, was used to destroy the anisotropy of the polarizer

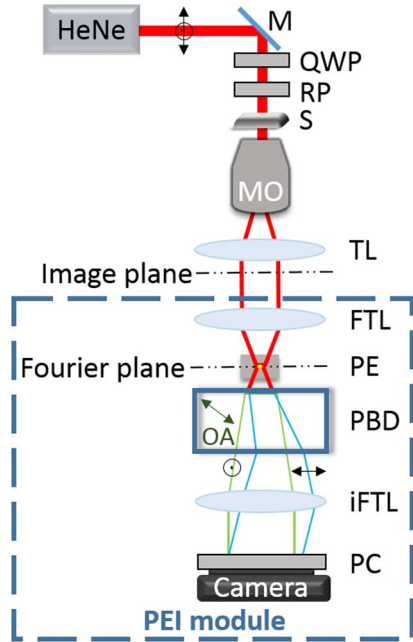


Fig. 1. PEI module, marked by a dashed blue rectangle, connected at the output port of an inverted microscope. The black arrows and circled dot represent polarization states. The red lines represent the light path from the laser through the sample. The green and blue lines show polarization displacement by the PBD. M, mirror; QWP, quarter wave plate; RP, rotating polarizer; S, sample; MO, microscope objective; TL, tube lens; FTL, Fourier transforming lens; PE, polarization encoding spatial filter; and PBD, birefringent polarizing beam displacer. The green arrow indicates the PBD optic axis (OA); iFTL, (inverse) Fourier transforming lens; PC, polarization combiner.

in a small central round spot of $14\ \mu\text{m}$ diameter. This created a nonpolarizing pinhole at the center of the element. Thus, horizontally polarized light is unaffected by the PE [see Fig. 2(a)], while vertically polarized light passes only through the pinhole area [see Fig. 2(b)].

Figures 2(c) and 2(d) show the imaged Fourier plane of the sample beam and the reference beam, respectively, in the two polarization states. Both low and high spatial frequencies are encoded into the sample beam and are transmitted through the PE in the horizontal polarization state [90° , see Fig. 2(c)]. On the other hand, in the vertical polarization state, only the pinhole transmits the light [0° , see Fig. 2(d)] and, thus, in the reference beam

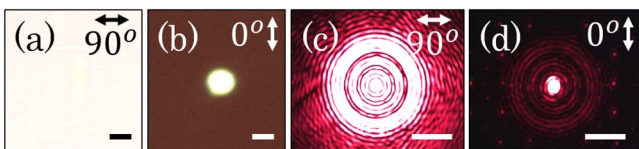


Fig. 2. (a),(b) Microscope image of the PE with (a) a co-polarized analyzer and (b) a cross-polarized analyzer. The scale bars are $14\ \mu\text{m}$. (c),(d) the imaged Fourier plane of the PE with (c) co-polarized analyzer and (d) a cross-polarized analyzer. The scale bars indicate $1 \cdot 10^{-3}\ \mu\text{m}^{-1}$. The arrows represent the analyzer polarization. 90° , horizontal polarization; 0° , vertical polarization.

polarization, only low spatial frequencies of the sample are transmitted.

From the PE, the light propagates toward a birefringent polarizing beam displacer (PBD) made from a calcite crystal (BD27, Thorlabs), which creates a $2.7\ \text{mm}$ displacement between the reference and sample beams [23]. Both beams are Fourier transformed back by iFTL lens ($75\ \text{mm}$ focal length) onto the digital camera (DCC1545M, Thorlabs), while creating $\sim 2^\circ$ off-axis angle between the sample and reference beams. Finally, to enable interference between the two orthogonal polarizations, we incorporated a polarization combiner (PC, polarizer rotated at -45°) before the camera. The carrier fringe period is determined by the off-axis angle, so that it allows three pixels per period, enabling full separation of the sample wave front without wasting camera pixels. The lateral resolution of the PEI system is limited by the lateral resolution of the inverted microscope, which in our setup was $1.5\ \mu\text{m}$.

The interferogram I , created on the digital camera sensor, can be mathematically expressed as follows: $I = |E_S|^2 + |E_R|^2 + E_S^* \cdot E_R + E_S \cdot E_R^*$, where the asterisk represents complex conjugate, and E_S and E_R are the sample and reference waves projected onto the detector, respectively. The first two terms on the right-hand side of the equation are the wave intensities, which, in the Fourier domain, represent the autocorrelations of the sample and reference beams. The last two terms represent the cross-correlations, and encode the phase accumulated at each point on the sample. To extract the phase map, we used the off-axis Fourier-based algorithm [24], which includes Fourier transform, filtering one of the cross-correlation terms, inverse Fourier transform, and phase unwrapping of the argument of the resulting matrix, to resolve 2π phase ambiguities [25]. To compensate for aberrations and field curvatures, we subtracted from the wrapped phase (before unwrapping) the wrapped phase extracted from an interferogram acquired with no sample. The unwrapped phase is proportional to the OPD of the sample [11].

To test the proposed system, we first used it to image the OPD map of a USAF 1951 phase test target. Figures 3(a) and 3(b) show intensity images of the sample at the two polarization states (by placing the polarizer in front of the camera at 0° or at 90°). To achieve contrast of the phase target, the image was slightly defocused. In the horizontal polarization [Fig. 3(a)], it can be seen that all sample features are clearly seen; therefore, the horizontal polarization carries the sample information. On the vertical polarization [Fig. 3(b)], all sample-related information is erased; therefore, this polarization can be used as the reference beam. A zoom-in image of the off-axis interference pattern acquired by the camera is seen in Fig. 3(c). The reconstructed phase map is shown in Fig. 3(d). The theoretical phase, φ , of the test target can be calculated by its thickness ($h = 120\ \text{nm}$), the refractive indices' difference between the sample ($n = 1.56$) and surrounding air ($n = 1$), and the wavelength ($\lambda = 632.8\ \text{nm}$), as follows: $\varphi = 2\pi \cdot \Delta n \cdot h / \lambda$. Therefore, the theoretical phase is $\sim 0.67\ \text{rad}$, which agrees with the measurements. Note that this target thickness was not precisely constant on all high spatial points because of the lithography process.

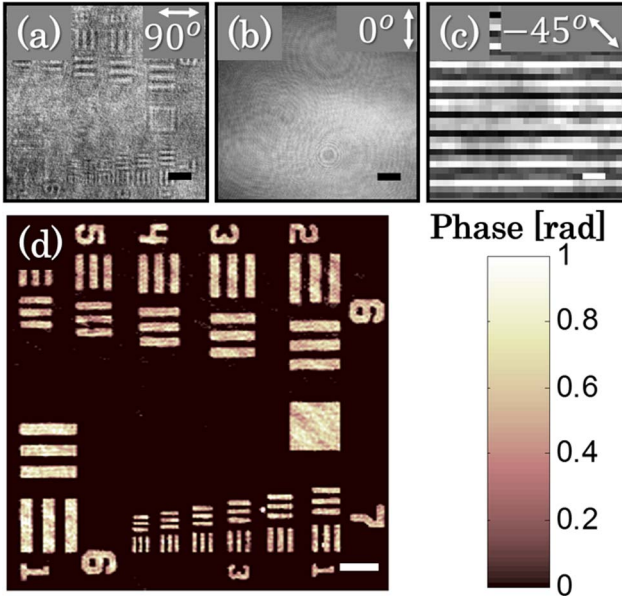


Fig. 3. Imaging of USAF 1951 phase test target using the PEI. (a) The intensity image with the co-polarized analyzer (at 90°), associated with the sample arm, and (b) with the cross-polarized analyzer (at 0°), associated with the reference arm. (c) The off-axis interference obtained on a small area of the background. (d) The reconstructed quantitative phase map. The scale bars are $26.7 \mu\text{m}$ in (a), (b), and (d), and $6.8 \mu\text{m}$ in (c).

In the proposed PEI, the polarization angle of the illumination affects the reconstruction quality by modifying the fringe contrast (FC). $\text{FC} = (I_{\max} - I_{\min}) / (I_{\max} + I_{\min})$, where I_{\max} and I_{\min} denote the maximum and minimum grayscale intensities of the interferogram, respectively. FC can also be calculated by the amplitude ratio of the cross-correlation terms and the autocorrelation terms of Eq. (1), that is, the ratio between the ac and the dc components of the interferogram [3]. The optimal FC is 1, and it is obtained when the amplitudes of the interfering beams are equal at the interference plane. Since the polarization angle sets the relative amplitudes of light in the reference and sample arms, it can be adjusted to obtain this optimal FC. Let P denote the power emerging from the laser and θ denote the source polarization angle with respect to the vertical axis. Then, according to Malus's law [26], $P_R(\theta) = \cos^2(\theta) \cdot P$ is the power fraction in the vertical polarization and $P_S(\theta) = \sin^2(\theta) \cdot P$ is the power fraction in the horizontal polarization. When passing through the PE, the horizontally polarized light remains unchanged, while the vertically polarized light is spatially filtered; therefore, its total power is reduced. If we consider a Gaussian distribution, the effective transmitted power is $P_R(\theta, R_1) = [1 - \exp(-2R_1^2/R_2^2)] \cdot \cos^2(\theta) \cdot P$, where R_1 is the aperture radius and R_2 is the waist radius of the focused beam (full width at half-maximum) [26]. After propagating through iFTL lens, the intensities of the sample and reference beams at the interference plane are inversely proportional to the collimated spot area. At this plane, the reference and sample spots radii are given by $R_R = \lambda \cdot f_2 / (\pi \cdot R_1)$ and $R_S = \lambda \cdot f_2 / (\pi \cdot R_2)$, respectively [25]. Therefore, the reference and sample beam intensities, projected onto the digital camera sensor, are given by

$I_R(\theta, R_1) = P_R(\theta, R_1) / (\pi \cdot R_R^2)$ and $I_S(\theta) = P_S(\theta) / (\pi \cdot R_S^2)$, correspondingly. Since the intensities are quadratically proportional to the fields, the theoretical FC as a function of the source polarization angle and the aperture radius for the PEI module is given by

$$\begin{aligned} \text{FC}_{\text{PEI}}(\theta, R_1) &= \frac{2|E_S(\theta) \cdot E_R^*(\theta, R_1)|}{|E_R(\theta, R_1)|^2 + |E_S(\theta)|^2} \\ &= \frac{2\sqrt{I_S(\theta) \cdot I_R(\theta, R_1)}}{I_R(\theta, R_1) + I_S(\theta)}. \end{aligned} \quad (1)$$

For airy disk radius at the Fourier plane, which was measured as $10 \mu\text{m}$, the effective beam waist radius, R_2 , is $13 \mu\text{m}$. Hence, the calculated optimal FC is obtained for source polarization angles of $\pm 20^\circ$. To check it experimentally, we acquired interferograms for different illumination polarization angles. For these measurements, the polarizer at the laser output was rotated at 5° steps and a set of interferograms was recorded. At polarization angles close to $\theta = 0^\circ$, measurements were recorded more frequently. For each polarization angle, FC was calculated and the phase map was reconstructed. Figure 4(a) presents the experimental and theoretical FC results which are in a good agreement. The optimal experimental FC was 0.8, and was obtained for source polarization angles of $\pm 20^\circ$. Figures 4(b)–4(e) show the

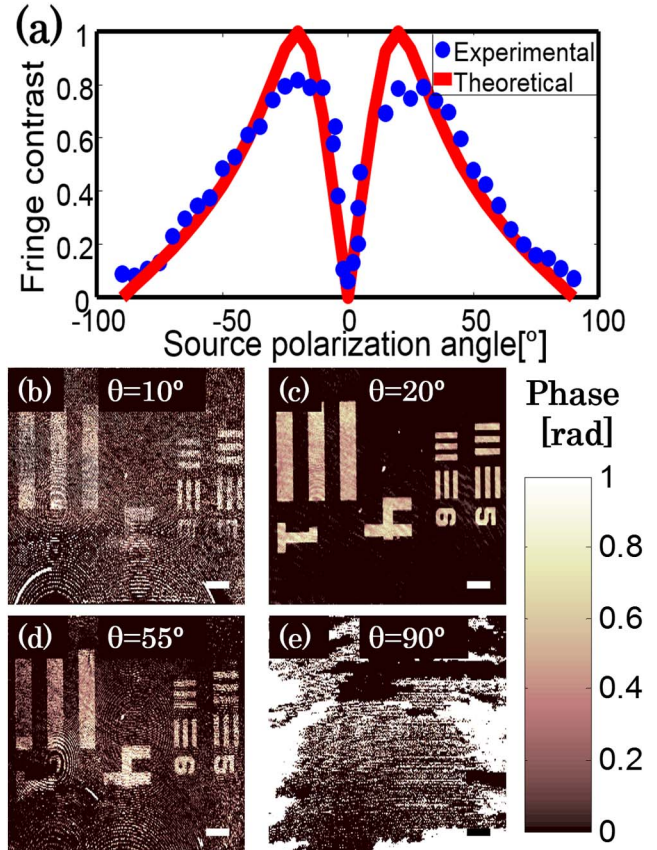


Fig. 4. Fringe contrast (FC) analysis: (a) experimental and theoretical FC of interferograms recorded with different source polarization angles. (b)–(e) The reconstructed quantitative phase maps for different input polarization angles: (b) 10° , (c) 20° , (d) 55° , and (e) 90° . Scale bars are $40 \mu\text{m}$.

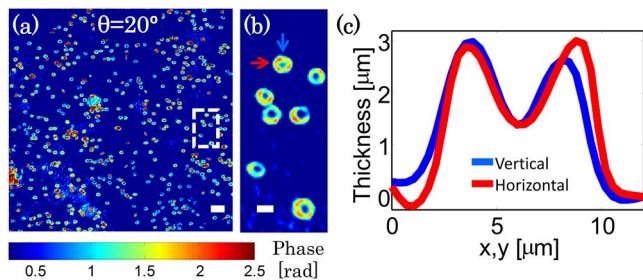


Fig. 5. (a) Quantitative phase map of human RBCs. The scale bar is 25 μm . (b) the zoom-in of the region marked by a white rectangle in (a). The scale bar is 8.4 μm . (c) The vertical and horizontal thickness profile cross sections through an RBC, indicated by arrows in (b).

reconstructed phase maps for several input polarization angles. As the fringe contrast decreases, the reconstruction quality deteriorates. When the laser is vertically or horizontally polarized, no interference is obtained, causing ambiguous reconstructed phase maps [see Figs. 4(e)].

To evaluate the temporal sensitivity of our setup, we built a conventional Mach-Zehnder interferometer [2] (MZI) on the same optical table. The temporal stability of the reconstructed phase of the PEI and MZI were 1.1 and 1.8 nm, respectively, which corresponds to $\sim 40\%$ improvement in the PEI configuration. The PEI stability can be further improved by combining the PEI elements together to reduce the relative phase jitter. The spatial sensitivity of the PEI was 1.85 nm.

We used the system to measure quantitative phase maps of human red blood cells (RBCs), diluted in phosphate buffer solution [see Figs. 5(a) and 5(b)]. The source polarization angle was set to $\theta = 20^\circ$, which enables optimal FC. To evaluate cell thickness, we assumed refractive indices of the cells and the solution as 1.40 and 1.33411, respectively [27]. Figure 5(c) shows the cell thickness profile assessments from horizontal (red) and vertical (blue) cross sections, at the locations indicated by arrows in Fig. 5(b), which fit previous measured RBC quantitative phase profiles [14,15,18].

In conclusion, we proposed a compact polarization-encoded, close-to-common-path, off-axis interferometer, with adjustable fringe contrast, for single-exposure quantitative phase imaging. The fringe contrast can be optimized by setting the input polarization angle, so that the reference and the sample beam intensities are equal at the interference plane. The system was demonstrated by quantitative phase imaging of both a USAF 1951 phase test target and an RBC sample. The ability to obtain optimal interference fringe modulation depth at two different source polarizations adds a degree of freedom to the measurement that might allow extracting of both the OPD and the polarization properties of the sample.

This work was supported partly by the European Commission Marie Curie Career Integration grant no. 333821 and the Israeli Science Foundation grant

no. 1331/13. We thank Pinhas Girshovitz for preparing the test target and for useful discussions.

References

1. R. Guo, B. Yao, P. Gao, J. Min, M. Zhou, J. Han, X. Yu, X. Yu, M. Lei, S. Yan, Y. Yang, D. Dan, and T. Ye, *Appl. Opt.* **52**, 8233 (2013).
2. P. Girshovitz and N. T. Shaked, *Opt. Express* **21**, 5701 (2013).
3. J. Dyson, *Interferometry as a Measuring Tool* (The Machinery, 1970).
4. J. Han, P. Gao, B. Yao, Y. Gu, and M. Huang, *Appl. Opt.* **50**, 2793 (2011).
5. V. Mico, Z. Zalevsky, and J. García, *Opt. Commun.* **281**, 4273 (2008).
6. E. Mihaylova, *Holography—Basic Principles and Contemporary Applications* (InTech, 2013), pp. 353–377.
7. Z. Monemhaghdoost, F. Montfort, Y. Emery, C. Depeursinge, and C. Moser, *Opt. Express* **19**, 24005 (2011).
8. P. Marquet, B. Rappaz, and P. Magistretti, *Opt. Lett.* **30**, 468 (2005).
9. M. Georges, J. Vandenrijt, and C. Thizy, *Appl. Opt.* **52**, A102 (2013).
10. J. Kühn, F. Charrière, T. Colomb, E. Cuche, F. Montfort, Y. Emery, P. Marquet, and C. Depeursinge, *Meas. Sci. Technol.* **19**, 074007 (2008).
11. J. Rosen, *Holography, Research and Technologies* (InTech, 2011), pp. 219–236.
12. Y. L. Lee, Y. C. Lin, H. Y. Tu, and C. J. Cheng, *J. Opt.* **15**, 025403 (2013).
13. G. Popescu, Y. Park, W. Choi, R. R. Dasari, M. S. Feld, and K. Badizadegan, *Blood Cells. Mol. Dis.* **41**, 10 (2008).
14. Y. Park, M. Diez-Silva, G. Popescu, G. Lykotrafitis, W. Choi, M. S. Feld, and S. Suresh, *Proc. Natl. Acad. Sci. USA* **105**, 13730 (2008).
15. G. Popescu, T. Ikeda, C. A. Best, K. Badizadegan, R. R. Dasari, and M. S. Feld, *J. Biomed. Opt.* **10**, 060503 (2005).
16. Y. Park, C. A. Best, K. Badizadegan, R. R. Dasari, M. S. Feld, T. Kuriabova, M. L. Henle, A. J. Levine, and G. Popescu, *Proc. Natl. Acad. Sci. USA* **107**, 6731 (2010).
17. G. Popescu, *Methods in Cell Biology*, 1st ed. (Elsevier, 2008), Vol. **90**, pp. 87–115.
18. H. Byun, T. R. Hillman, J. M. Higgins, M. Diez-Silva, Z. Peng, M. Dao, R. R. Dasari, S. Suresh, and Y. Park, *Acta Biomater.* **8**, 4130 (2012).
19. N. Shaked and L. Satterwhite, *Biomed. Opt. Express* **1**, 706 (2010).
20. C. S. Anderson, *Appl. Opt.* **34**, 7474 (1995).
21. D. Wang, Y. Yang, C. Chen, and Y. Zhuo, *Appl. Opt.* **50**, 2342 (2011).
22. R. N. Smartt and W. H. Steel, *J. Opt. Soc. Am.* **62**, 737 (1972).
23. S. Kocsis, B. Braverman, S. Ravets, M. J. Stevens, R. P. Mirin, L. K. Shalm, and A. M. Steinberg, *Science* **332**, 1170 (2011).
24. P. Girshovitz and N. Shaked, *Opt. Lett.* **39**, 2262 (2014).
25. M. D. P. Dennis and C. Ghiglia, *Two-Dimensional Phase Unwrapping: Theory, Algorithms, and Software* (Wiley, 1998).
26. B. Saleh and M. Teich, *Fundamentals of Photonics*, 2nd ed. (Wiley-Interscience, 1991).
27. R. L. Schoch, L. E. Kapinos, and R. Y. H. Lim, *Proc. Natl. Acad. Sci. USA* **109**, 16911 (2012).